ARTICLE

Photocurrent Generation in Nanostructured Organic Solar Cells

Fan Yang[†,‡] and Stephen R. Forrest[‡,*]

[†]Department of Electrical Engineering, Princeton University, Princeton, New Jersey 08544 and [‡]Department of Electrical Engineering & Computer Science, Materials Science & Engineering, and Physics, University of Michigan, Ann Arbor, Michigan 48109

ABSTRACT Photocurrent generation in nanostructured organic solar cells is simulated using a dynamical Monte Carlo model that includes the generation and transport properties of both excitons and free charges. Incorporating both optical and electrical properties, we study the influence of the heterojunction nanostructure (*e.g.*, planar vs bulk junctions) on donor−acceptor organic solar cell efficiencies based on the archetype materials copper phthalocyanine (CuPc) and C_{60}. Structures considered are planar and planar-mixed heterojunctions, homogeneous and phase-separated donor−acceptor (DA) mixtures, idealized structures composed of DA pillars, and nanocrystalline DA networks. The thickness dependence of absorption, exciton diffusion, and carrier collection efficiencies is studied for different morphologies, yielding results similar to those experimentally observed. The influences of charge mobility and exciton diffusion length are studied, and optimal device thicknesses are proposed for various structures. Simulations show that, with currently available materials, nanocrystalline network solar cells optimize both exciton diffusion and carrier collection, thus providing for highly efficient solar energy conversion. Estimations of achievable energy conversion efficiencies are made for the various nanostructures based on current simulations used in conjunction with experimentally obtained fill factors and open-circuit voltages for conventional small molecular weight materials combinations.

KEYWORDS: photovoltaics · organic semiconductors · donor−acceptor heterojunction · exciton · charge collection · Monte Carlo simulation

The power conversion efficiency of organic photovoltaic (OPV) cells has significantly increased since the introduction of the donor−acceptor (DA) heterojunction (HJ).[1] In this structure, photogenerated excitons diffuse to the heterointerface where they are dissociated into free electrons and holes. In archetype planar heterojunctions (PHJs), the exciton dissociation efficiency (η_{ED}) is limited by their short diffusion length, L_D, which is typically between 3 and 40 nm.[2] The bulk heterojunction (BHJ) solar cell circumvents the exciton diffusion limitation in PHJ structures by introducing a dispersed DA interface with a large surface area.[3,4] In BHJ cells, excitons can easily reach a local DA interface, although isolated islands and cul-de-sacs formed during phase separation between the D and A materials can reduce the carrier collection efficiency (η_{CC}) in both polymeric[5] and small molecular weight[6] solar cells.

A fundamental understanding of the exciton and carrier transport properties of these various structures remains incomplete. For example, the continuum approximation used in many computational studies[2,7,8] is inadequate to fully describe the complex excitonic and electronic interactions in the presence of nanoscale morphological texture. Watkins *et al.* have proposed a dynamical Monte Carlo (DMC) model that treats exciton diffusion and carrier collection in a mixed DA structure, and they found a tradeoff between η_{ED} and η_{CC} with increasing interface area.[9] A similar DMC model has also been applied to study charge separation and recombination in planar and mixed HJs.[10] However, these models have not included optical interference effects that have been shown to play an important role in determining both exciton generation and dissociation.[2,11] The effects of variations in electron (μ_n) and hole (μ_p) mobilities have also been neglected in past work, although in practical organic solar cells, μ_n and μ_p may differ by several orders of magnitude,[12,13] which significantly impacts the charge separation process.[14]

Here we introduce a comprehensive microscopic DMC model that includes the effects of optical interference, energetic disorder, exciton Föster energy transfer, Onsager exciton dissociation, carrier transport, electrostatic interactions, and carrier mobilities. To provide comparisons of calculations with experiment, many parameters used are characteristic of the archetype copper phthalocyanine (CuPc)/C_{60} HJ system that employs an indium−tin oxide (ITO) anode and Ag cathode. The device performance is then modeled for several HJ morphologies and structures.

This paper is organized as follows: In Theory of Photocurrent Generation, we

*Address correspondence to stevefor@umich.edu.

Received for review December 29, 2007 and accepted March 31, 2008.

Published online May 2, 2008.
10.1021/nn700447t CCC: $40.75

© 2008 American Chemical Society

briefly describe the principles of photocurrent generation at a DA HJ. Methods used for simulating HJ morphologies demonstrated in recent experimental studies are presented in Heterojunction Morphology. Also, the DMC model of exciton and carrier generation and transport is described in Exciton and Charge Transport. The simulation results are provided in Results and Discussion. We discuss the dependence of photocurrent generation on material phase separation, nanoscale heterointerface structure, carrier mobility and exciton diffusion length. In addition, the power conversion efficiency limits of organic solar cells are considered based on experimentally obtained fill factors and open-circuit voltages for conventional small molecular weight materials combinations. We summarize this work in Conclusions. The Methods are briefly described, with details of the derivation of η_{ED} and η_{CC} from the DMC data given in the Appendix.

THEORY OF PHOTOCURRENT GENERATION

Detailed descriptions of photocurrent generation in organic solar cells can be found in several reviews;[2,13,15] here we give only a brief introduction to the process. Upon absorption, an exciton is generated, which then diffuses to the DA interface, where it dissociates into a free electron and hole. Alternatively, the exciton is quenched and releases energy in the form of a phonon. Starting at a DA interface, the electrons and holes diffuse through the acceptor and donor materials, respectively, to the collecting electrodes, providing current to a load in the external circuit. If a free carrier collides with a nearby charge of opposite sign, they recombine.

It is convenient to break this optical-to-electrical conversion process into four steps:[2] (1) absorption of a photon and the generation of an exciton, (2) exciton diffusion, (3) exciton dissociation into a free electron and hole by charge transfer, and (4) charge collection by the anode (holes) and cathode (electrons). The external quantum efficiency of the solar cell is η_{EQE}, defined as the ratio of the number of electron−hole pairs collected at the electrodes to the number of incident photons, *viz.*,

$$\eta_{EQE} = \eta_\alpha \eta_{IQE} = \eta_\alpha \eta_{ED} \eta_{CT} \eta_{CC} \quad (1)$$

where η_α, η_{ED}, η_{CT}, and η_{CC} are the absorption, exciton diffusion, charge transfer, and carrier collection efficiencies, respectively, and η_{IQE} is the internal quantum efficiency. Typically, $\eta_{CT} = 1$ in organic DA solar cells due to the rapidity (∼10−100 fs) of the process. Hence, an estimation of η_{EQE} requires only determination of the remaining three components, η_α, η_{ED}, and η_{CC}.[2]

HETEROJUNCTION MORPHOLOGY

Here we develop energy-based models that qualitatively reproduce HJ morphologies observed in the CuPc/C_{60} system. In the following section, we will use these derived morphologies to track and understand the dependence of exciton and charge transport on film structure. Six morphology types are studied: a conventional PHJ,[1,16] a homogeneous DA mixture,[17] a BHJ based on DA material phase separation,[6,18] a planar-mixed HJ (PM-HJ),[19] an idealized BHJ consisting of pillars arranged in a chessboard pattern with top and bottom buffer layers,[9,10,20] and a random nanocrystalline network.[21] The PHJ cell consists of two homogeneous layers separately comprised of D and A molecules. The PM-HJ cell is comprised of a DA mixed layer sandwiched between top and bottom continuous homogeneous layers. The chessboard morphology consists of alternating square pillars of equal size. The uniformly space-filling pillars are sandwiched between continuous homogeneous layers.[10] Except where otherwise stated, the pillar widths are chosen to be smaller than the minimum exciton diffusion length, L_D, leading to efficient exciton dissociation and charge transfer.[22]

For simplicity, simulations of organic thin-film structures assume a cubic lattice with lattice constant a on the order of a molecular diameter (typically ∼1 nm). The simulation lattices are $(100a)^2$ in the substrate ($x-y$) plane, with varying depth in the substrate normal (z) direction for studying thickness-dependent device behavior. The bottom and top of the lattice are assumed to contact the anode and the exciton blocking layer,[16] respectively. Periodic boundary conditions are applied. To approximate the HJ morphology, donor and acceptor molecules are represented by assigning lattice sites with "spins" of +1 and −1, respectively.[9,23]

Mixed Heterojunction. Phase separation from the homogeneous mixture is generated using an entropy-driven site spin exchange Ising model[9,10] with parameters adjusted to reproduce the observed grain size and distribution for binary phase mixtures.[6,23] Lattice sites are allowed to exchange their spins between all 26 proximate neighbors (6 in the ⟨100⟩ direction, 12 in the ⟨110⟩ direction, and 8 in the ⟨111⟩ direction). Since the van der Waals (vdW) interaction between like molecules is much larger than the interaction between different molecules,[24] the change in system energy that results from the exchange of two neighboring spins is represented using the Ising Hamiltonian for the energy of site, i:[23]

$$W_i = -\frac{1}{2}\sum_j (\delta_{S_i S_j} - 1) \quad (2)$$

where $\delta_{S_i S_j}$ is the Kronecker delta for spins occupying sites i and j. Exchange attempts between sites i and j are accepted with the probability $P(\Delta W_{ij})$, following Kawasaki spin-exchange dynamics:[25]

$$P(\Delta W_{ij}) = \frac{\exp(-\Delta W_{ij}/k_B T)}{1 + \exp(-\Delta W_{ij}/k_B T)} \quad (3)$$

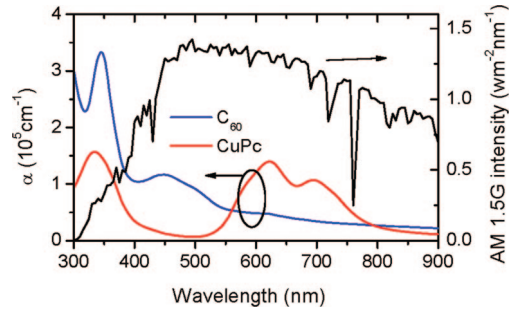

Figure 1. Absorption coefficients, α, of CuPc and C_{60} films on Si substrates, compared to the standard AM1.5G solar irradiation spectrum. Solar spectrum from ref 37.

TABLE 1. Material Properties of CuPc and C_{60}

property	CuPc	C_{60}	ref
relative dielectric constant (ε_r)	3.5	3.5	
energy width of density of states (σ_E, eV)	0.03	0.03	33, 34
exciton diffusion length (L_D, nm)	15	40	2
exciton lifetime ($\tau_{exciton}$, s)	1×10^{-8}	1×10^{-6}	2
exciton binding energy (E_{EB}, eV)	0.5	0.5	39
exciton dissociation rate (w_{ed}, s^{-1})	1×10^{13}	1×10^{13}	60
carrier mobility (μ, $cm^2 V^{-1} s^{-1}$)	7×10^{-4}	5×10^{-2}	12, 61
carrier recombination rate (w_{cr}, s^{-1})	5×10^5	5×10^5	10

Here, k_B is Boltzmann's constant, T is the temperature, and $\Delta W_{ij} = W_j - W_i$. This procedure leads to a large-scale phase separation occurring in a system with limited miscibility,[23] as is the case for CuPc/C_{60}. The accepted spin exchanges tend to form aggregates of like molecules by lowering the total system energy, while the grain size is controlled by the number of executed spin exchanges.

Nanocrystalline Heterojunction. The growth of the more complex DA nanocrystalline network[21] is modeled assuming growth by alternate deposition of ultrathin layers of D and A molecules, taking into account gas-phase transport, surface diffusion, and evaporation back into the gas phase.[26] The structural morphology is simulated on the basis of the vdW interaction using the atom−atom potential method.[24,27] Specifically, the total bond potential between neighboring molecules i and j is $\Phi_{ij} = \Sigma\varphi_{m(i)n(j)}$, where $\phi_{m(i)n(j)}$ is the potential between the mth and nth atoms in molecules i and j, respectively, given by

$$\varphi_{m(i)n(j)} = -\alpha_{mn}/r^6_{m(i)n(j)} + \beta_{mn}\exp(-\gamma_{mn} r_{m(i)n(j)}) \quad (4)$$

where $r_{m(i)n(j)}$ is the distance between atoms m and n, and α, β, and γ are vdW constants.[24,28] The energy of molecule i, ε_i, is then obtained by summing over all neighboring molecules j.

Following this procedure, the interaction energies between molecules are $\varepsilon = 0.867$ eV (for CuPc−CuPc bonds),[29] $\varepsilon = 1.5$ eV (C_{60}−C_{60}),[30,31] and $\varepsilon = 0.044$ eV (CuPc−C_{60}).[32] We assume that the organic molecules are randomly generated in the gas phase at a distance $>2000a$ from the substrate. The molecule then diffuses along the solid surface, moving from unoccupied site i to j, at a rate

$$K_{i\to j} = \nu f(\Delta\varepsilon_{ij}) \quad (5)$$

where ν is the lattice vibration factor, $\Delta\varepsilon_{ij} = \varepsilon_j - \varepsilon_i$, and

$$f(\Delta\epsilon_{ij}) = \begin{cases} \exp\left(-\dfrac{\Delta\epsilon_{ij}}{k_B T}\right) & \text{if } \Delta\epsilon_{ij} > 0 \\ 1 & \text{if } \Delta\epsilon_{ij} < 0 \end{cases} \quad (6)$$

Due to the relative bond energies given above, similar molecules tend to preferentially aggregate, forming extended domains. The surface molecule can also reevaporate back into the gas phase when the destination site, j, is above the solid surface, with $\varepsilon_j = 0$.

To approximate the actual nanocrystalline morphology, the first homogeneous layer consists of D molecules. Following that, a thin A layer is deposited, forming aggregates that do not provide full coverage of the underlying D layer. A second, thin D layer is then deposited to partially cover the A layer, but it also directly contacts the first, continuous D layer. Similarly, several thin, discontinuous DA layer pairs are deposited, followed by a thick and continuous A capping layer.

EXCITON AND CHARGE TRANSPORT

Exciton and carrier transport by short-range hopping between localized states[9] are simulated in the HJ structures presented in Heterojunction Morphology using the DMC algorithm known as the first reaction method (FRM). In FRM, the probability of an allowed process is calculated after the first time the particle (*i.e.*, an exciton or charge) appears and is updated following exciton dissociation, quenching, bimolecular recombination, or charge collection. Compared to a full DMC calculation in which the probability is recalculated after each change of system configuration, FRM significantly reduces computation time. We checked the validity of the FRM model by comparing it to the full DMC model for all morphologies exposed to 1 W/cm^2 (10 sun intensity) air mass (AM) 1.5 global illumination, and the difference between the two models was <0.5%. The agreement results because the exciton (10^{17} cm^{-3}) and carrier (5×10^{17} cm^{-3}) densities in organic solar cells, even at high intensity, are low, and hence interparticle interactions are seldom affected by the change of system configuration. The energy disorder is simulated by assigning each lattice site a random energy, E, following a Gaussian distribution with a half-width of $\sigma_E = 30$ meV.[33,34] In Table 1, we list all materials properties of CuPc and C_{60} used in the simulation.

The exciton generation rate depends on the optical properties of the solar cell, which behaves as a weak

and lossy microcavity.[2] The optical field intensity is calculated as a function of incident wavelength, λ, over the range 300 nm $< \lambda <$ 900 nm, as well as a function of distance from the reflective cathode, following the transfer matrix method.[2] Extinction coefficients and indices of refraction of CuPc and C_{60} thin films are measured as functions of λ with 50-nm-thick films on Si substrates by ellipsometry, and used in the calculations. In planar structures, interfaces between different layers are assumed to be optically flat, as the root-mean-square (rms) roughness of the ITO substrates and organic thin films is typically smaller than a few nanometers.[35,36] Effects of the ITO-coated glass substrate are included by correcting for reflections at the air/substrate and substrate/organic interfaces, assuming an incident AM1.5G spectrum (Figure 1).[2,37] Then, the exciton generation rate, r_{eg}, is the product of the optical field intensity in the microcavity and the wavelength-dependent material absorption coefficients. The absorption coefficients of CuPc and C_{60} measured with thin films grown on fused quartz substrates are shown in Figure 1.

The FRM simulation generates excitons at rates consistent with the incident light intensity and spectrum, and tracks their diffusion to the DA HJ, where they dissociate into free carriers. The carrier generation and transport model is similar to that used by Watkins *et al.*,[9] with the addition of Onsager exciton dissociation and carrier quenching at the electrodes.

To approximate Föster energy transfer that governs exciton diffusion, the exciton hopping time, τ_{eh}, depends on the distance, R_{ij}, between the original and destination molecules, *i* and *j*, and the difference in *i* and *j* hopping site energies, ΔE_{ij}, *viz*:[33]

$$\tau_{eh} = -\tau_{ex}\left(\frac{R_{ij}}{L_D}\right)^6 \frac{\ln(X)}{f(\Delta E_{ij})} \qquad (7)$$

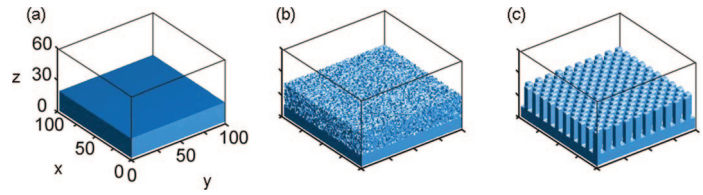

Figure 2. Typical donor−acceptor (DA) morphologies. (a) Planar heterojunction (PHJ); (b) planar-mixed heterojunction (PM-HJ); (c) chessboard-type HJ with pillar widths of 5*a*, with a lattice constant *a*. The total film thicknesses in all morphologies are 60*a*, in which only the donor phase is displayed. The acceptor phase is transparent for clarity. Morphologies shown in (b) and (c) have continuous D (10*a*) and A (30*a*) layers at the bottom and top surfaces, respectively.

Here, τ_{ex} is the exciton lifetime, and $0 < X < 1$ is a random number. The hopping probability is then

$$f(\Delta E_{ij}) = \begin{cases} \exp(-\dfrac{\Delta E_{ij}}{k_B T}) & \text{if } \Delta E_{ij} > 0 \\ 1 & \text{if } \Delta E_{ij} \leq 0 \end{cases} \qquad (8)$$

where ΔE_{ij} includes the change of site energy, the Coulomb interaction between neighboring charges, the built-in potential determined by the organic film thickness, and the work function difference between anode and cathode. Onsager's theory[38] is applied to describe exciton dissociation, where the generated carrier gains energy[14] equal to the difference between the DA energy offset and the exciton binding energy. This is approximately 0.5 eV for CuPc and C_{60}.[39]

Assuming the effective-medium theory, the carrier hopping time is determined by [9,40]

$$\tau_{ch} = \frac{qa^2 \exp(4aR_{ij} - 4a^2)}{6k_B T \mu_{n(p)}} \frac{1}{f(\Delta E_{ij})} \qquad (9)$$

To maintain computational efficiency, the Coulomb interaction is vectorially summed within a $(9a)^3$ neighborhood, which for $a \approx 1$ nm is more than twice the Debye length (4 nm) typical of organic materials. Free

TABLE 2. Average Domain Size, Specific Interface Area, and Cell Efficiencies of Mixed Films before and after Annealing at Different Numbers of MC Steps for a 100 × 100 × 60 nm³ Lattice

MC steps	0	1	10	50	100
Morphology	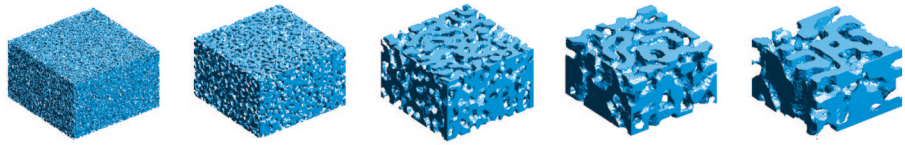				
Domain size (*a*)	0.98± 0.02	2.02± 0.04	4.9± 0.1	7.9± 0.2	10.3± 0.7
Specific interface area (a^2)	61.22±0.03	29.70±0.06	12.2±0.1	7.6±0.3	6±1
η_{CC}	0.31±0.01	0.34±0.01	0.40±0.01	0.44±0.02	0.43±0.01
η_{ED}	1.00±0.01	1.0±0.01	0.97±0.01	0.93±0.01	0.87±0.02
η_{IQE}	0.31±0.01	0.34±0.01	0.39±0.01	0.41±0.02	0.37±0.02

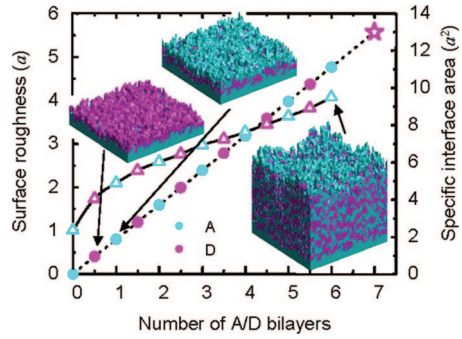

Figure 3. Simulation of the growth progression of a D(10*a*)/[A(3*a*)/D(3*a*)]$_6$ network. The plot shows the root-mean-square (rms) surface roughness (open triangles) and the specific interface area (filled circles) as functions of the number of acceptor (A) and donor (D) bilayers. The star shows the final area ratio after the six-period network is covered by a continuous acceptor layer. The three inset diagrams show the evolution of the film structure and surface morphology of the A and D nanocrystals at different growth stages in the progression, where 3-D interconnected networks can be clearly seen (see ref 21).

charge diffuses to the adjacent electrodes where they are collected, with mobilities given in Table 1.

RESULTS AND DISCUSSION

Heterojunction Morphology. The PHJ, PM-HJ, and chessboard structures with total film thicknesses of 60 nm are shown schematically in Figure 2. The PHJ structure is composed of two continuous layers: D (20 nm) and A (40 nm) (Figure 2a). The PM-HJ (Figure 2b) and chessboard (Figure 2c) structures both assume similar bottom D (10 nm) and top A (30 nm) layers. The intermediate layer in the PM-HJ structure sandwiched between these uniform layers consists of a 20-nm-thick, 1:1 DA mixed layer. The intermediate layer in the chessboard HJ is composed of an array of equally spaced 5 nm square pillars.

The 60-nm-thick homogeneous and mixed HJ morphologies (Table 2) are simulated using the method described in the Heterojunction Morphology section under "Mixed Heterojunction". One Monte Carlo (MC) step occurs when the number of executed site (*i.e.*, spin) exchanges equals the total number of lattice sites.[9] The average domain size is calculated as half the ratio of the total volume to the total DA interface area. Furthermore, the specific interface area is defined as the ratio of the total interface area to interface area projected onto the *xy* plane. After 1, 10, 50, and 100 MC steps, a series of phase-separated morphologies develops, yielding increasing grain size and decreasing specific interface area. The homogeneous mixed film has an average domain size of *a*, implying a highly dispersed mixture with minimal phase segregation. Annealing at high *T* lowers the total system energy, resulting in domain sizes of 2*a* after 1 MC step and 5*a* after 10 MC steps. The domain size increases gradually to 10*a* after 100 MC steps, similar to domain sizes obtained in annealed, organic solar cells.[6,18] As a result of the domain growth, the specific interface area decreases from $61a^2$ to $6a^2$.

The simulated morphology of the nanocrystalline HJ network D(10*a*)/[A(3*a*)/D(3*a*)]$_6$/A(30*a*) is shown in Figure 3. Here, the notation [A(d_1)/D(d_2)]$_l$ refers to the average thicknesses, d_1 and d_2, of the A and D layers, respectively, and *l* is the integer number of DA pairs. Domains are continuous along the *z*-direction, with an average domain size of 6.3 ± 0.4 nm for the morphology shown in Figure 3, matching that observed in CuPc/C_{60} nanocrystalline networks.[21] The intermediate layer lacks continuous pathways to the adjoining homogeneous D and A caps when $d_i > 20a$, in agreement with the experimental result that the network structures form when $d_i \leq 15$ nm (15*a*).[21] The specific interface area increases monotonically, and reaches $9.6a^2$ after the sixth DA pair is grown, comparable to that obtained in the annealed structure after 10−50 MC steps (Table 2). The surface rms roughness of the HJ structure also increases with the number of DA pairs, thus requiring a thicker top continuous layer for planarization.

Initial Carrier Separation following Exciton Dissociation. After exciton dissociation and prior to bimolecular charge recombination, the initial separation distance of generated carriers is found to be between *a* and 10*a*, in agreement with photoconductivity data.[41] If Onsager theory is ignored, the oppositely charged carriers accumulate at each side of the DA HJ, forming a dipole. For example, less than 0.5% of the photogenerated charges diffuse away from a DA interface under illumination of 100 mW/cm^2, except when very thin DA layers are used (*e.g.*, total thickness $d < 10$ nm). Hence, the carrier recombination rate approaches the carrier generation rate, leading to $\eta_{CC} \approx 0$. By comparison, in mixed DA cells, carrier generation is dispersed throughout the film, resulting in a lower concentration than that at a PHJ heterointerface.[9,10] When Onsager effects are neglected, the germinate recombination efficiency, η_{GR}, is high ($\eta_{GR} > 34\%$ in a PHJ and $\eta_{GR} > 85\%$ in a mixed HJ),[10] whereas in our simulation, $\eta_{GR} < 3\%$ for all structures, which is consistent with experimental observation.[42]

Space-Charge Build-Up. The number of charges generated, n_g, the number of free charges in the active layer, *n*, and the numbers of collected electrons, $n_{e,c}$, and holes, $n_{h,c}$, are determined using the method in the Appendix, with results plotted in Figure 4a for a typical CuPc(20 nm)/C_{60}(40 nm) PHJ cell under 1 W/cm^2 (10 suns), AM 1.5G illumination. At the onset of the simulation, *n* increases with time until a steady state is reached at time t_0. In this example, $t_0 \approx 25$ μs and $\eta_{CC} = 1$. From the similar slopes of the curves for both holes and electrons, we infer balanced carrier collection *rates*. However, at $t > t_0$, the difference between $n_{e,c}(t)$ and $n_{h,c}(t)$ suggests that the number of collected electrons is equal to the total number of collected holes plus those holes remaining within the organic film (Figure

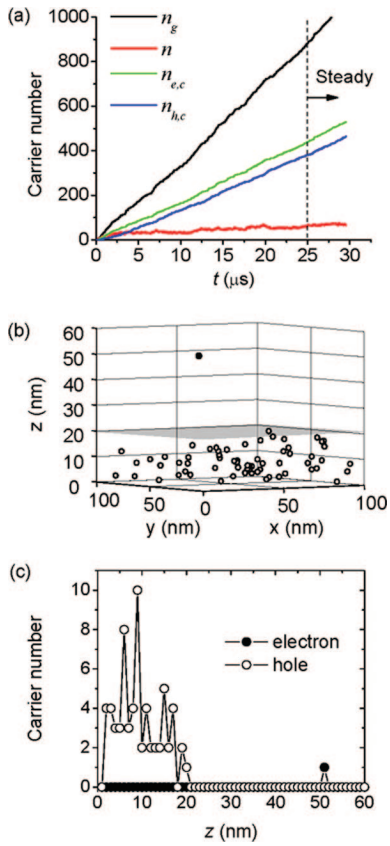

Figure 4. (a) Simulated exciton and carrier number as functions of time, *t*, in a 100 nm × 100 nm lattice, recorded for a CuPc(20 nm)/C_{60}(40 nm) solar cell under 1000 mW/cm^2 (10 sun), AM 1.5G illumination. The total numbers of generated carriers, n_g, carriers within the organic films, *n*, collected electrons, $n_{e,c}$, and collected holes, $n_{h,c}$, are plotted as functions of *t*. (b) Electrons and holes in the organic film in steady state. The shadow indicates the planar DA interface separating the bottom CuPc and top C_{60} layers. (c) Charge distribution in the substrate normal (*z*) direction in the film shown in (b).

4b) as a result of their lower mobility in the donor (CuPc). The excess hole population disappears shortly after the light is turned off, leading to $n = 0$ and $n_{e,c} = n_{h,c}$.

The steady-state charge carrier distribution normal to the substrate surface (*i.e.*, along *z*) is plotted in Figure 4c. From Poisson's equation, a maximum field, $F_{max} = 3.35 \times 10^6$ V/m, is generated at the DA interface, resulting in a space-charge-induced potential of $V_{SC} = 0.037$ V, opposite to the built-in HJ field. Figure 5 shows F_{max} and V_{SC} in a PHJ (CuPc(20 nm)/C_{60} (40nm)) and a mixed (60 nm, homogeneous CuPc:C_{60} = 1:1) cell at an incident power of $0.1 < P_0 < 1000$ mW/cm^2. In the PHJ cell, there is significant space-charge build-up at $P_0 > 10$ mW/cm^2, resulting in $F_{max} = 6 \times 10^5$ V/m and $V_{SC} = 5$ mV at 100 mW/cm^2. The space-charge region is limited to CuPc, with no charge build-up in the C_{60} layer since the electron mobility in C_{60} is greater than the hole mobility in CuPc. In contrast, in the mixed HJ, the space charge is dispersed throughout the organic film. In addition, the space-charge concentration is higher in the mixed cell due to less effective charge transport. Hence, in the mixed film, $F_{max} = 1.10 \times 10^7$ V/m at 100 mW/cm^2 (Figure 5a), which is more than 100 times higher than in a PHJ cell of the same thickness. The large space-charge field results in $V_{SC} = 0.42$ V in the mixed film, which can appreciably impact charge collection. When the light intensity is increased to 1000 mW/cm^2, $V_{SC} = 1.5$ V (Figure 5b). A fit of log(V_{SC}) vs log(P_0) gives a linear relationship, yielding slopes of between 0.55 and 0.6. Theoretical calculation predicts a slope of 0.5, and polymeric DA mixed cells have shown a measured slope of 0.51.[43]

Under high light intensity, a space-charge region forms in all of the simulated morphologies, thereby reducing the charge collection efficiency. This results in both lower η_{CC} and open-circuit voltage, V_{OC}, as confirmed in small molecular weight[44] and polymer/fullerene cells.[45,46]

Dependence of the Photocurrent on Morphology. Phase separation in homogeneous DA mixtures has been widely used as a means to increase η_{CC} while preserving high η_{ED} in both polymeric and small molecular weight solar cells.[6,18,47] We studied 60-nm-thick CuPc:C_{60} (1:1) DA mixtures under 100 mW/cm^2 (1 sun), AM 1.5G solar illumination after undergoing a range of annealing MC steps (see Table 2). Here, the charge collection efficiency increases from $\eta_{CC} = 0.31$ in a homogeneous mixture to $\eta_{CC} = 0.44$ in an annealed film after 50 MC steps, and then rolls off as the domain size grows for 100 MC steps, consistent with observation.[18,47] Increasing phase-separated domain size, on the other hand, results in a decrease in η_{ED}. After 100 MC steps, the domain size (10 nm) approaches $L_D^{CuPc} = 15$ nm, and η_{ED} drops to <0.9. As a result of increased η_{CC} and decreased η_{ED}, phase separation increases η_{IQE} from 0.31 in the homogeneous mixture, peaking at $\eta_{IQE} = 0.41$ in annealed morphologies at 50 MC steps (Table 2). The simulations show that although phase separation and domain growth in a homogeneous DA mixture can significantly improve η_{IQE}, the thermodynamically driven

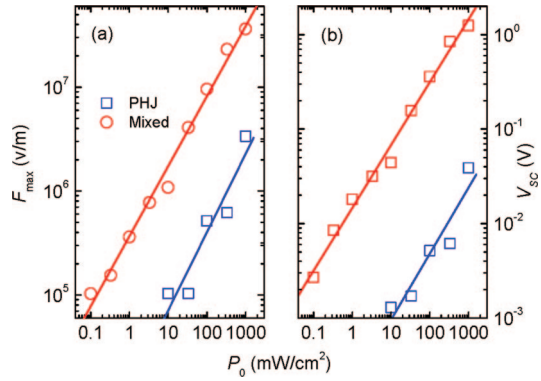

Figure 5. Space-charge-induced (a) maximum field, F_{max}, and (b) potential, V_{SC}, opposite to the built-in potential as functions of light intensity, P_0. The PHJ cell structure is CuPc(20 nm)/C_{60}(40 nm), and the mixed cell is comprised of a 60-nm-thick CuPc:C_{60} (1:1) homogeneously mixed film.

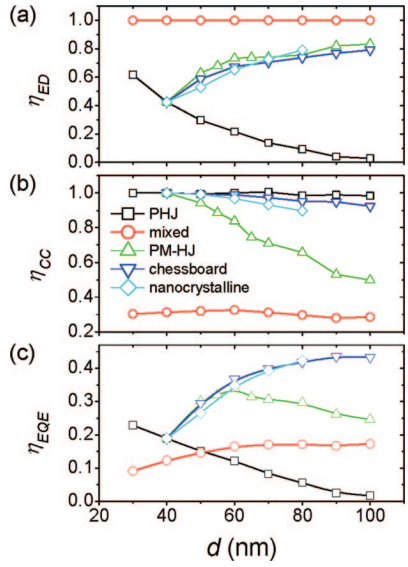

Figure 6. Efficiencies of CuPc/C_{60} solar cells with different morphologies (following Figure 2, Figure 3, and Table 2). (a) Exciton diffusion efficiency, η_{ED}, (b) charge collection efficiency, η_{CC}, and (c) external quantum efficiency, η_{EQE}, plotted as functions of the total organic layer thickness, *d*. The PHJ cell has the structure of CuPc(d_0 nm)/C_{60}(d_0 +20 nm). The PM-HJ, chessboard, and nanocrystalline network structures are comprised of a 10-nm-thick bottom CuPc layer and a 30-nm-thick top C_{60} layer. The square pillar width in the chessboard structure is 5 nm. The nanocrystalline structure is CuPc(10 nm)/[C_{60}(3 nm)/CuPc(3 nm)]$_l$/C_{60}(30 nm), where *l* = 0, 2, 4, 6, and 8.

process inevitably results in isolated islands of one or both of the constituent materials, leading to a saturation in efficiency improvement.[6,18,48]

The efficiencies of cells with different morphologies are compared in Figure 6. The η_α values for the several structures considered (not shown) are nearly identical as expected, increasing from $\eta_\alpha = 0.37 \pm 0.2$ in 30-nm-thick films to 0.6 ± 0.1 in 80-nm-thick films and then decreasing as the optical interference peak shifts away from the organic active layers. In contrast, η_{ED} and η_{CC} are strongly dependent on different DA morphologies (Figure 6a,b). For example, assuming that $L_D^D = 15$ nm and $L_D^A = 40$ nm (Table 1), η_{ED} in the PHJ structure decreases from >0.6 in CuPc(10 nm)/C_{60}(20 nm) to $\eta_{ED} = 0.2$ in CuPc(20 nm)/C_{60}(40 nm), and approaches $\eta_{ED} \cong 0$ for $d > 100$ nm as a result of the limited interface area in a PHJ structure. In contrast, the mixed HJ cell has $\eta_{ED} = 1$ for all thicknesses due to the highly distributed DA interface. In the remaining three structures—the PM-HJ, chessboard, and nanocrystalline network—$\eta_{ED} = 0.4$ for CuPc(10 nm)/C_{60}(30 nm) and increases with thickness, approaching η_{ED} in the mixed structure. In these three structures, $\eta_{ED} = 0.8$ at $d = 100$ nm.

A principal result of this analysis is shown in Figure 6c, where we show η_{EQE} for different morphologies calculated using eq 1. The PHJ and mixed cells have a low η_{EQE} due to their low η_{ED} and η_{CC}, respectively. In the PM-HJ cells,[19,49] the maximum η_{EQE} is obtained in a CuPc(10 nm)/CuPc:C_{60}(20 nm)/C_{60}(30 nm) cell, which corresponds to the experimentally optimized structure.[19] In nanocrystalline cells with the structure of CuPc(10 nm)/[C_{60}(3 nm)/CuPc(3 nm)]$_l$/C_{60}(30 nm), η_α increases from 0.45 at $l = 0$ ($d = 40$ nm) to 0.6 at $l = 6$ ($d = 76$ nm). However, η_{EQE} increases by 120%, from <0.2 to 0.45 over the same range of *d*, implying that nanocrystalline networks located in the region of maximum optical field are highly efficient. Good agreement is achieved between the simulated η_{EQE} and those measured in fabricated devices for various morphologies, as summarized in Table 3. Indeed, we find that the efficiencies of nanocrystalline networks are nearly identical to that of the idealized chessboard structure when the morphological scale is on the same order as the exciton diffusion length.

TABLE 3. Comparison between Simulated and Observed η_{EQE} for Various CuPc/C_{60} Solar Cells

HJ structure	simulated η_{EQE}	measured η_{EQE}	ref
PHJ: CuPc(20 nm)/C_{60}(40 nm)	0.13	0.14 ± 0.1	21
		0.15 ± 0.1	16, 62
mixed HJ: CuPc:C_{60}(60 nm)	0.16	0.16 ± 0.1[a]	49
nanocrystalline network HJ: CuPc(10 nm)/[C_{60}(3 nm)/CuPc(3 nm)]$_6$/C_{60}(30 nm)	0.42	0.43 ± 0.2	21

[a]Calculated from the reported $J_{SC} = 4.8$ mA/cm^2 measured under 100 mW/cm^2, AM 1.5G irradiation.

Effects of Carrier Mobility. To investigate the effects of carrier mobility, μ_n and μ_p are varied from 1×10^{-7} to 5 cm^2 V^{-1} s^{-1}, encompassing the practical range accessible to organic materials useful in PV cell applications. The exciton diffusion lengths are taken as $L_D^D =$ 15 nm and $L_D^A =$ 40 nm, which along with other material properties typical of CuPc and C_{60} are listed in Table 1.

The simulated η_{CC} *vs* μ_n and μ_p is shown in Figure 7. In the PHJ cells (Figure 7a), $\eta_{CC} = 1$ for $\mu_{n,p} > 2 \times 10^{-4}$ cm^2 V^{-1} s^{-1}, where the carriers can move rapidly toward the electrodes with no significant carrier recombination. For $\mu_{n,p} < 10^{-4}$ cm^2 V^{-1} s^{-1}, the rate of carriers diffusing from the DA interface is smaller than their generation rate. This leads to a slower extraction of charges, and hence space-charge build-up (*c.f.* Figure 5), resulting in increased bimolecular recombination at the heterointerface. Indeed, for $\mu_{n,p} < 5 \times 10^{-7}$ cm^2 V^{-1} s^{-1}, $\eta_{CC} \cong 0$.

Compared to a PHJ, the mixed HJ structure (Figure 7b) has a significantly lower $\eta_{CC} < 0.4$, resulting from a larger recombination rate at the increased interface area. In the mixed HJ cell, Langevin bimolecular recombination dominates, where the recombination rate is proportional to the carrier mobility.[50,51] Hence, a higher $\mu_{n,p}$ increases both the extraction and recombination of carriers.[46] Our simulation shows that the peak $\eta_{CC} =$

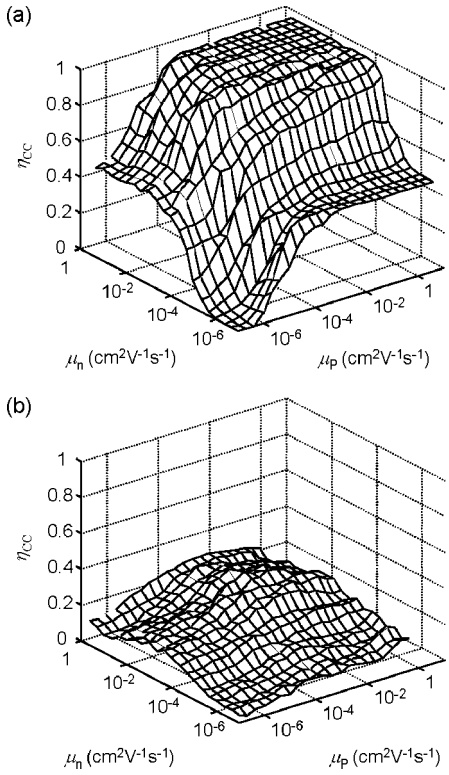

Figure 7. Influence of carrier mobilities, μ_n and μ_p, on η_{CC} in (a) ITO/D(20 nm)/A(40 nm)/BCP/Ag PHJ and (b) ITO/D:A(60 nm)/BCP/Ag mixed solar cells. Other material parameters are provided in Table 1.

0.4 occurs at $\mu_{n,p} \approx 10^{-2}$ cm^2 V^{-1} s^{-1}, decreasing for both higher and lower charge mobilities. Similar optimal $\mu_{n,p}$ values have been calculated for polymer blend cells.[50]

These findings provide guidance in the selection of DA materials for mixed structures, where η_{IQE} is primarily limited by η_{CC}.[52] Although CuPc:C_{60} mixtures have demonstrated efficient solar cells with short circuit densities, $J_{SC} > 5.5$ mA/cm^2 under 100 mW/cm^2, AM1.5G irradiation,[17,49] some materials combinations, *e.g.*, CuPc:3,4,9,10-perylenetetracarboxylic bis-benzimidazole (PTCBI), have significantly reduced photocurrents ($J_{SC} = 15$ μA/cm^2).[6] The carrier mobilities of bulk organic materials are determined by the proximity of neighboring molecules and the overlap of π-bonds between neighbors. Molecular stacking and hence the extent of bond overlap are disrupted in the amorphous mixed layers.[6,12] Due to the higher symmetry of C_{60} molecules, use of this molecule as an acceptor in mixed films therefore leads to enhanced transport over planar acceptor molecules such as PTCBI, where the π-bond overlap is significantly reduced by wider molecular separation and oblique orientation. Indeed, our simulations show that the CuPc:PTCBI film experiences space-charge build-up due to the lower μ_n than in C_{60}, leading to $\eta_{CC} < 0.1$ (Figure 7b). Furthermore, a 10-fold increase of J_{SC} was attributed to an increase in μ_p from 4×10^{-8} to 1×10^{-4} cm^2 V^{-1} s^{-1} in polymer-based solar cells.[53]

Efficiency Limits of DA Heterojunction Cells. The principles used to model the CuPc/C_{60} system are applicable to small-molecule and polymer-based materials systems in general. Hence, these findings have consequences in the design of the structure and the selection of materials for efficient DA junction solar cells. Here we investigate the influence of L_D on efficiencies and determine the film thickness and morphological texture required to optimize organic solar cells. For this calculation, we assume absorption coefficients of $\alpha_D = \alpha_{CuPc}$ and $\alpha_A = \alpha_{C_{60}}$, mobilities of $\mu_p^D = \mu_n^A = 5 \times 10^{-2}$ cm^2 V^{-1} s^{-1}, and exciton diffusion lengths $L_D^D = L_D^A$. Then, η_{EQE} is calculated under 100 mW/cm^2 (1 sun), AM 1.5G illumination, as shown in Figure 8.

As expected, η_{EQE} in the PHJ structure (Figure 8a) shows a strong dependence on L_D. At $L_D = 500$ nm, $\eta_{IQE} = 1.0$ for $d < 200$ nm, resulting in $\eta_{EQE} = \eta_\alpha$. At larger thicknesses, absorption shifts toward the ITO/organic interface, where the narrow exciton distribution results in a decreased η_{ED}, and hence η_{EQE}. The highest efficiency ($\eta_{EQE} = 0.71$) is achieved for $d = 300$ nm.

In the homogeneous DA mixed cell (Figure 8b), the peak $\eta_{EQE} = 0.27$ at $d = 300$ nm and does not depend on L_D since $\eta_{ED} = 1$. In the chessboard structure with 5-nm-wide pillars (Figure 8c), η_{EQE} has little dependence on L_D, as expected. The optimal η_{EQE} is achieved for $d \approx 250$ nm in Figure 8c. Similar efficiencies are calculated in chessboard structures with pillar widths less than L_D (Figure 8d). Lower η_{EQE} results when the pillar

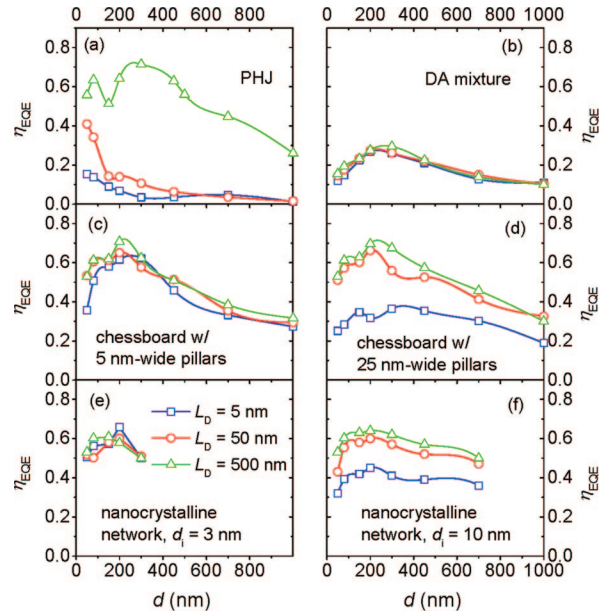

Figure 8. Calculated η_{EQE} dependence on exciton diffusion length, L_D (L_D = 5, 50, and 500 nm), and device thickness, *d*, for (a) PHJ, (b) homogeneous DA mixture, chessboard structures with (c) 5-nm-wide and (d) 25-nm-wide pillar arrays, and nanocrystalline networks of D(10 nm)/[A(d_i)/D(d_i)]$_i$/A(20 nm) where (e) d_i = 3 nm and (f) d_i = 10 nm. The *d* ranges in the nanocrystalline network (e,f) are limited to the onset of a root-mean-square surface roughness greater than 50 nm.

TABLE 4. Comparison of Several HJ Morphologies

	PHJ	homogeneous mixed HJ	annealed mixed HJ	PM-HJ	chessboard	nanocrystalline network
morphological characteristics	continuous layers with flat interface	dispersed DA interface in the whole volume	random domains with islands and cul de sacs	DA mixture sandwiched between DA continuous layers	alternating D and A pillars sandwiched between DA layers	interconnected network of nanocrystallites
advantages	high η_{CC}	simple structure and high η_{ED}	improved η_{CC} over homogeneous mixed HJ	improved η_{ED} over PHJ	ideal structure with high η_{CC} and high η_{ED}	high η_{CC} and η_{ED}
efficiency limiting factor	L_D	lack of continuous conductive pathways; limited by μ	carrier trapping within islands; limited by μ	limited by L_D or μ	ideal structure	film thickness limited by surface roughness

width (25 nm) is larger than L_D (5 nm). We also compare nanocrystalline cells with DA layer thicknesses of $d_i = 3$ nm and $d_i = 10$ nm, yielding average domain sizes of 6.3 ± 0.6 and 22 ± 3 nm, respectively, as shown in Figure 8e,f. When $d_i > 15$ nm, continuous DA layers are obtained, forming multilayer structures that block carrier collection.[54] Similar to the chessboard structure, the highest η_{ED} is obtained when the domain size is less than L_D (Figure 8e). The optimal $\eta_{EQE} = 0.64$ is achieved at $d = 200$ nm, with $\eta_{ED} = 1$ and $\eta_{IQE} \cong 1$. The total organic layer thickness in the nanocrystalline cells is, however, limited due to the monotonically increasing[21] rms surface roughness >50 nm, at $d > 300$ nm and $d > 700$ nm for $d_i = 3$ nm and $d_i = 10$ nm, respectively. Such a rough film surface results in shorts across the active organic region. Hence, the efficiency of the nanocrystalline cells may ultimately be limited by surface roughness, which requires control over organic molecular crystallization.[20]

The optimal efficiency of $\eta_{EQE} \cong 0.7$ is obtained in the chessboard and nanocrystalline networks, with domain sizes equal to or smaller than L_D. Using practically available materials with $L_D = 15$ nm,[2,13] $\eta_{EQE} = 0.63$ is achievable in the nanocrystalline cell, corresponding to $J_{SC} = 20.8$ mA/cm^2 under 100 mW/cm^2, AM 1.5G illumination. Experiments show that the V_{OC} and FF of nanocrystalline cells show little dependence on light intensity, implying minimum carrier recombination at the DA interface. If we assume $V_{OC} = 0.5$ V and a fill factor, FF =0.57, typically observed for CuPc/C_{60}-based nanocrystalline solar cells,[21] the best device would have a power conversion efficiency of $\eta_P = 6\%$.[55]

Combining the simulation results shown in Results and Discussion, high-efficiency solar cells ($\eta_{EQE} \geq 0.6$) must have a large $\mu_{n,p}$ to achieve $\eta_{CC} = 1$ and L_D larger than or comparable to that of the domain size to obtain a high η_{ED}. Although the DA mixed film has been widely used, its efficiency is inherently limited by a low η_{CC} (*cf.* Figure 7b). The simulations show that the nanocrystalline network is the most promising means for achieving high η_{EQE} and hence J_{SC} in organic solar cells, considering that the optimal chessboard structures require a precise arrangement of nanoscale features that may be difficult to achieve.

The absorption coefficient of organic materials determines the photon absorption and exciton generation profile, thus imposing conditions that lead to an optimal active layer thickness. For the structures and materials discussed in this work, the optimal layer thickness is between 200 and 300 nm. Efficient PHJ cells also rely on the use of DA materials with large L_D, of which very few have been thus far identified. Increases in L_D have focused on improving the exciton lifetime and mobility. In fact, $L_D = 40$ nm is obtained in C_{60}, due to the generation of long-lived triplet states following optical absorption. In addition, long-range crystalline order favors more efficient energy transfer, hence resulting in an increased L_D.[56,57] Improvement in η_P also relies on a high V_{OC}, which is determined by, among other factors, the energetic structure of the DA heterointerface[39,58] and can be increased by using the tandem architecture.[11,59]

CONCLUSIONS

A dynamical Monte Carlo model is developed to simulate organic solar cells with nanoscale morphologies. The model includes effects of optical interference and exciton and carrier transport. The model reveals the formation of space-charge regions in low-mobility organic materials. The simulated η_{EQE} is similar to experimentally obtained values in cells with a variety of morphologies. Absorption by the organic layers limits the optimal cell thicknesses to between 200 and 300 nm. The highest η_{EQE} is achieved in chessboard and nanocrystalline networks, where the domain size is equal to or smaller than L_D. Based on observed V_{OC} and FF for nanocrystalline CuPc/C_{60} solar cells, our calculations suggest that these structures have the potential to achieve a power conversion efficiency of $\eta_P = 6\%$ under 1 sun, AM 1.5G illumination. A detailed comparison of the structural characteristics, advantages, and efficiency limiting factors of the six morphologies is given in Table 4.

Our model applies to both small molecular weight and polymer cells with various morphologies. It provides a detailed understanding of the energy conversion process in nanoscale structures and should aid in the design and optimization of OPV cells.

METHODS

The simulation codes for nanomorphology generation and DMC energy conversion were written in C++ and compiled using Microsoft Visual C++ 6.0. Each DMC simulation took 0.5−20 h, depending on different morphologies, when running on personal computers equipped with Pentium Core Duo 2 GHz processors. The simulation terminates as judged by the method described in the Appendix. Three-dimensional nanomorphologies are generated by the C++ codes and plotted using Matlab.

APPENDIX

To determine the exciton dissociation and carrier collection efficiencies, the simulation records the carrier number, n, at every carrier collection event and records the ensemble [n_1, n_2, n_3, ..., n_{500}] for the previous 500 carrier events. The ratio

$$\rho = \frac{\sigma(n_1,\ n_2,\ n_3,\ \ldots,\ n_{500})}{\text{average}(n_1,\ n_2,\ n_3,\ \ldots,\ n_{500})} \qquad \text{(A1)}$$

is then calculated, where σ is the standard deviation of the ensemble. Our simulation assumes the system is stable when $\rho < 0.01$. After the system reaches steady state, 2000 extra carrier collection events are then simulated. The numbers of excitons and carriers are recorded as functions of t, with the exciton diffusion efficiency equal to the ratio of the slopes of the number of excitons dissociated per unit time to those generated, *viz.*:

$$\eta_{ED} = \frac{S(n_{exc,dissoc}(t))}{S(n_{exc,gen}(t))} \qquad \text{(A2)}$$

The carrier collection efficiency, η_{CC}, is then

$$\eta_{CC} = \frac{S(n_{e,c}(t)) + S(n_{h,c}(t))}{2S(n_{exc,dissoc}(t))} \qquad \text{(A3)}$$

for $t > t_0$, where $S(n(t))$ is the slope of $n(t)$.

Acknowledgment. The authors gratefully acknowledge the Air Force Office of Scientific Research and Global Photonic Energy Corp. for partial support of this work.

REFERENCES AND NOTES

1. Tang, C. W. Two-Layer Organic Photovoltaic Cell. *Appl. Phys. Lett.* **1986**, *48*, 183–185.
2. Peumans, P.; Yakimov, A.; Forrest, S. R. Small Molecular Weight Organic Thin-Film Photodetectors and Solar Cells. *J. Appl. Phys.* **2003**, *93*, 3693–3723.
3. Yu, G.; Gao, J.; Hummelen, J. C.; Wudl, F.; Heeger, A. J. Polymer Photovoltaic Cells: Enhanced Efficiencies Via a Network of Internal Donor-Acceptor Heterojunctions. *Science* **1995**, *270*, 1789–1791.
4. Halls, J. J. M.; Walsh, C. A.; Greenham, N. C.; Marseglia, E. A.; Friend, R. H.; Moratti, S. C.; Holmes, A. B. Efficient Photodiodes from Interpenetrating Polymer Networks. *Nature* **1995**, *376*, 498–500.
5. Hoppe, H.; Niggemann, M.; Winder, C.; Kraut, J.; Hiesgen, R.; Hinsch, A.; Meissner, D.; Sariciftci, N. S. Nanoscale Morphology of Conjugated Polymer/Fullerene-Based Bulk-Heterojunction Solar Cells. *Adv. Funct. Mater.* **2004**, *14*, 1005–1011.
6. Peumans, P.; Uchida, S.; Forrest, S. R. Efficient Bulk Heterojunction Photovoltaic Cells Using Small-Molecular-Weight Organic Thin Films. *Nature* **2003**, *425*, 158–162.
7. Barker, J. A.; Ramsdale, C. M.; Greenham, N. C. Modeling the Current-Voltage Characteristics of Bilayer Polymer Photovoltaic Devices. *Phys. Rev. B* **2003**, *67*, 075205.
8. Gommans, H. H. P.; Kemerink, M.; Kramer, J. M.; Janssen, R. A. J. Field and Temperature Dependence of the Photocurrent in Polymer/Fullerene Bulk Heterojunction Solar Cells. *Appl. Phys. Lett.* **2005**, *87*, 122104.
9. Watkins, P. K.; Walker, A. B.; Verschoor, G. L. B. Dynamical Monte Carlo Modeling of Organic Solar Cells: The Dependence of Internal Quantum Efficiency on Morphology. *Nano Lett.* **2005**, *5*, 1814–1818.
10. Marsh, R. A.; Groves, C.; Greenham, N. C. A Microscopic Model for the Behavior of Nanostructured Organic Photovoltaic Devices. *J. Appl. Phys.* **2007**, *101*, 083509.
11. Maennig, B.; Drechsel, J.; Gebeyehu, D.; Simon, P.; Kozlowski, F.; Werner, A.; Li, F.; Grundmann, S.; Sonntag, S.; Koch, M.; et al. Organic P-I-N Solar Cells. *Appl. Phys. A: Mater. Sci. Process.* **2004**, *79*, 1–14.
12. Rand, B. P.; Xue, J.; Uchida, S.; Forrest, S. R. Mixed Donor-Acceptor Molecular Heterojunctions for Photovoltaic Applications. I. Material Properties. *J. Appl. Phys.* **2005**, *98*, 124902.
13. Blom, P. W. M.; Mihailetchi, V. D.; Koster, L. J. A.; Markov, D. E. Device Physics of Polymer:Fullerene Bulk Heterojunction Solar Cells. *Adv. Mater.* **2007**, *19*, 1551–1566.
14. Peumans, P.; Forrest, S. R. Separation of Geminate Charge-Pairs at Donor-Acceptor Interfaces in Disordered Solids. *Chem. Phys. Lett.* **2004**, *398*, 27–31.
15. Gledhill, S. E.; Scott, B.; Gregg, B. A. Organic and Nano-Structured Composite Photovoltaics: An Overview. *J. Mater. Res.* **2005**, *20*, 3167–3179.
16. Peumans, P.; Forrest, S. R. Very-High-Efficiency Double-Heterostructure Copper Phthalocyanine/C_{60} Photovoltaic Cells. *Appl. Phys. Lett.* **2001**, *79*, 126–128.
17. Uchida, S.; Xue, J.; Rand, B. P.; Forrest, S. Organic Small Molecule Solar Cells with a Homogeneously Mixed Copper Phthalocyanine: C_{60} Active Layer. *Appl. Phys. Lett.* **2004**, *84*, 4218–4220.
18. Ma, W.; Yang, C.; Gong, X.; Lee, K.; Heeger, A. J. Thermally Stable, Efficient Polymer Solar Cells with Nanoscale Control of the Interpenetrating Network Morphology. *Adv. Funct. Mater.* **2005**, *15*, 1617–1622.
19. Xue, J.; Rand, B. P.; Uchida, S.; Forrest, S. R. A Hybrid Planar-Mixed Molecular Heterojunction Photovoltaic Cell. *Adv. Mater.* **2005**, *17*, 66–71.
20. Yang, F.; Shtein, M.; Forrest, S. R. Controlled Growth of a Molecular Bulk Heterojunction Photovoltaic Cell. *Nat. Mater.* **2005**, *4*, 37–41.
21. Yang, F.; Sun, K.; Forrest, S. R. Efficient Solar Cells Using All-Organic Nanocrystalline Networks. *Adv. Mater.* **2007**, *19*, 4166–4171.
22. Kannan, B.; Castelino, K.; Majumdar, A. Design of Nanostructured Heterojunction Polymer Photovoltaic Devices. *Nano Lett.* **2003**, *3*, 1729–1733.
23. Adams, C. D.; Srolovitz, D. J.; Atzmon, M. Monte Carlo Simulation of Phase Separation During Thin-Film Codeposition. *J. Appl. Phys.* **1993**, *74*, 1707–1715.
24. Forrest, S. R.; Zhang, Y. Ultrahigh-Vacuum Quasiepitaxial Growth of Model van der Waals Thin Films. I. Theory. *Phys. Rev. B* **1994**, *49*, 11297–11308.
25. Kawasaki, K. In *Phase Transitions and Critical Phenomena*; Domb, C., Green, M. S., Eds.; Academic: New York, 1972; Vol. 2.

26. Xiao, R.-F.; Alexander, J. I. D.; Rosenberger, F. Growth Morphologies of Crystal Surfaces. *Phys. Rev. A* **1991**, *43*, 2977–2992.
27. Kitaigorodsky, A. I. *Molecular Crystals and Molecules*; Academic: New York, 1973.
28. Abe, A.; Jernigan, R. L.; Flory, P. J. Conformational Energies of N-Alkanes and the Random Configuration of Higher Homologs Including Polymethylene. *J. Am. Chem. Soc.* **1966**, *88*, 631–639.
29. Liu, D.-J.; Selinger, R. L. B.; Weeks, J. D. Representing Molecular Shape and Interactions: A Reduced Intermolecular Potential for Copper Phthalocyanine. *J. Chem. Phys.* **1996**, *105*, 4751–4760.
30. Antropov, V. P.; Gunnarsson, O.; Jepsen, O. Coulomb Integrals and Model Hamiltonians for C_{60}. *Phys. Rev. B* **1992**, *46*, 13647–13650.
31. Lof, R. W.; van Veenendaal, M. A.; Koopmans, B.; Jonkman, H. T.; Sawatzky, G. A. Band Gap, Excitons, and Coulomb Interaction in Solid C_{60}. *Phys. Rev. Lett.* **1992**, *68*, 3924.
32. Fendrich, M.; Wagner, T.; Stohr, M.; Moller, R. Hindered Rotation of a Copper Phthalocyanine Molecule on C_{60}: Experiments and Molecular Mechanics Calculations. *Phys. Rev. B* **2006**, *73*, 115433–115437.
33. Scheidler, M.; Lemmer, U.; Kersting, R.; Karg, S.; Riess, W.; Cleve, B.; Mahrt, R. F.; Kurz, H.; Bässler, H.; Göbel, E. O.; et al. Monte Carlo Study of Picosecond Exciton Relaxation and Dissociation in Poly(Phenylenevinylene). *Phys. Rev. B* **1996**, *54*, 5536–5544.
34. Baldo, M. A.; Forrest, S. R. Transient Analysis of Organic Electrophosphorescence: I. Transient Analysis of Triplet Energy Transfer. *Phys. Rev. B* **2000**, *62*, 10958–10966.
35. Lewis, B. G.; Paine, D. C. Applications and Processing of Transparent Conducting Oxides. *MRS Bull.* **2000**, *25*, 22–27.
36. Yang, F.; Forrest, S. R. Organic Solar Cells Using Transparent SnO_2-F Anodes. *Adv. Mater.* **2006**, *18*, 2018–2022.
37. American Society for Testing and Materials. *Standard Tables for Reference Solar Spectral Irradiances: Direct Normal and Hemispherical on 37° Tilted Surface*; ASTM G173-03e1; ASTM International: West Conshohocken, PA, 2007. (www.astm.org).
38. Onsager, L. Initial Recombination of Ions. *Phys. Rev.* **1938**, *54*, 554–557.
39. Rand, B. P.; Burk, D. P.; Forrest, S. R. Offset Energies at Organic Semiconductor Heterojunctions and Their Influence on the Open-Circuit Voltage of Thin-Film Solar Cells. *Phys. Rev. B* **2007**, *75*, 115327.
40. Fishchuk, I. I.; Hertel, D.; Bässler, H.; Kadashchuk, A. K. Effective-Medium Theory of Hopping Charge-Carrier Transport in Weakly Disordered Organic Solids. *Phys. Rev. B* **2002**, *65*, 125201.
41. Silinsh, E. A.; Capek, V. *Organic Molecular Crystals: Interaction, Localization, and Transport Phenomena*; AIP Press: New York, 1994.
42. Zhang, F.; Jespersen, K. G.; Björström, C.; Svensson, M.; Andersson, M. R.; Sundström, V.; Magnusson, K.; Moons, E.; Yartsev, A.; Inganäs, O. Influence of Solvent Mixing on the Morphology and Performance of Solar Cells Based on Polyfluorene Copolymer/Fullerene Blends. *Adv. Funct. Mater.* **2006**, *16*, 667–674.
43. Mihailetchi, V. D.; Wildeman, J.; Blom, P. W. M. Space-Charge Limited Photocurrent. *Phys. Rev. Lett.* **2005**, *94*, 126602–126604.
44. Xue, J.; Rand, B. P.; Uchida, S.; Forrest, S. R. Mixed Donor-Acceptor Molecular Heterojunctions for Photovoltaic Applications. II. Device Performance. *J. Appl. Phys.* **2005**, *98*, 124903.
45. Koster, L. J. A.; Mihailetchi, V. D.; Xie, H.; Blom, P. W. M. Origin of the Light Intensity Dependence of the Short-Circuit Current of Polymer/Fullerene Solar Cells. *Appl. Phys. Lett.* **2005**, *87*, 203502.
46. Koster, L. J. A.; Mihailetchi, V. D.; Blom, P. W. M. Bimolecular Recombination in Polymer/Fullerene Bulk Heterojunction Solar Cells. *Appl. Phys. Lett.* **2006**, *88*, 052104.
47. Li, G.; Shrotriya, V.; Huang, J. S.; Yao, Y.; Moriarty, T.; Emery, K.; Yang, Y. High-Efficiency Solution Processable Polymer Photovoltaic Cells by Self-Organization of Polymer Blends. *Nat. Mater.* **2005**, *4*, 864–868.
48. Shaheen, S. E.; Brabec, C. J.; Sariciftci, N. S.; Padinger, F.; Fromherz, T. 2.5% Efficient Organic Plastic Solar Cells. *Appl. Phys. Lett.* **2001**, *78*, 841–843.
49. Sullivan, P.; Heutz, S.; Schultes, S. M.; Jones, T. S. Influence of Codeposition on the Performance of CuPc-C_{60} Heterojunction Photovoltaic Devices. *Appl. Phys. Lett.* **2004**, *84*, 1210–1212.
50. Mandoc, M. M.; Koster, L. J. A.; Blom, P. W. M. Optimum Charge Carrier Mobility in Organic Solar Cells. *Appl. Phys. Lett.* **2007**, *90*, 133504.
51. Langevin, P. Recombinaison et Mobilité des Ions Dans les Gaz. *Ann. Chim. Phys.* **1903**, *28*, 433–531.
52. Koster, L. J. A.; Smits, E. C. P.; Mihailetchi, V. D.; Blom, P. W. M. Device Model for the Operation of Polymer/Fullerene Bulk Heterojunction Solar Cells. *Phys. Rev. B* **2005**, *72*, 085205−085209.
53. Mihailetchi, V. D.; Xie, H. X.; de Boer, B.; Koster, L. J. A.; Blom, P. W. M. Charge Transport and Photocurrent Generation in Poly(3-Hexylthiophene): Methanofullerene Bulk-Heterojunction Solar Cells. *Adv. Funct. Mater.* **2006**, *16*, 699–708.
54. Peumans, P.; Bulovic, V.; Forrest, S. R. Efficient, High-Bandwidth Organic Multilayer Photodetectors. *Appl. Phys. Lett.* **2000**, *76*, 3855–3857.
55. Diehl, W.; Sittinger, V.; Szyszka, B. Thin Film Solar Cell Technology in Germany. *Surf. Coat. Technol.* **2005**, *193*, 329–334.
56. Gregg, B. A.; Sprague, J.; Peterson, M. W. Long-Range Singlet Energy Transfer in Perylene Bis(Phenethylimide) Films. *J. Phys. Chem. B* **1997**, *101*, 5362–5369.
57. Mäkinen, A. J.; Melnyk, A. R.; Schoemann, S.; Headrick, R. L.; Gao, Y. Effect of Crystalline Domain Size on the Photophysical Properties of Thin Organic Molecular Films. *Phys. Rev. B* **1999**, *60*, 14683–14687.
58. Koster, L. J. A. *Device Physics of Donor/Acceptor-Blend Solar Cells*; University of Groningen, Nijenborgh, 2007.
59. Kim, J. Y.; Lee, K.; Coates, N. E.; Moses, D.; Nguyen, T.-Q.; Dante, M.; Heeger, A. J. Efficient Tandem Polymer Solar Cells Fabricated by All-Solution Processing. *Science* **2007**, *317*, 222–225.
60. van Hal, P. A.; Janssen, R. A. J.; Lanzani, G.; Cerullo, G.; Zavelani-Rossi, M.; Silvestri, S. D. Full Temporal Resolution of the Two-Step Photoinduced Energy-Electron Transfer in a Fullerene-Oligothiophene-Fullerene Triad Using Sub-10 fs Pump-Probe Spectroscopy. *Chem. Phys. Lett.* **2001**, *345*, 33–38.
61. Gould, R. D. Structure and Electrical Conduction Properties of Phthalocyanine Thin Films. *Coord. Chem. Rev.* **1996**, *156*, 237–274.
62. Kanno, H.; Fujishima, D.; Shirakawa, M.; Kinoshita, T.; Maruyama, E.; Shibata, K.; Tanaka, M. Organic Thin-Film Solar Cell Employing a Novel Electron-Donor Material. Presented at 17th International Photovoltaic Science and Engineering Conference, Fukuoko, Japan, Dec 3−7, 2007; pp 275−276.